Implementation of the Peruvian Earthquake Early Warning System

Pablo Lara[1,2], Hernando Tavera[2], Quentin Bletery[1], Jean-Paul Ampuero[1], Adolfo Inza[2], David Portugal[2], Benazir Orihuela[3], and Fernando Meza[2]

[1]Observatoire de la Côte d'Azur, Université Côte d'Azur, IRD, CNRS, Géoazur, France
[2]Instituto Geofísico del Perú, Lima, Perú
[3]Swiss Seismological Service at ETH Zurich, Zurich, Switzerland

Corresponding author: Pablo Lara, `pablo.elara@ieee.org`

Abstract

We present the implementation and testing of the seismological components of the Peruvian Earthquake Early Warning System (Sistema de Alerta Sísmica Peruano, SASPe). SASPe is designed to send alert messages to areas located within a given distance from the epicenter of large (magnitude ≥ 6.0) subduction earthquakes, with a first alert based on data available 3 seconds after the arrival of the P wave on the nearest station. The system comprises a dedicated network of 111 strong-motion stations installed along the Peruvian coast. During over 2 years of testing, the magnitude estimates are virtually unbiased, with no false positives or false negatives. In the most critical virtual scenarios of earthquakes occurring within 57 km from populated areas, SASPe can provide user lead times of up to 8 seconds. For more distant areas (from 70 km to 120 km), lead times range from 10 to 20 seconds. Once the construction of the alert broadcasting system by the civil defense authority is finalized, SASPe will provide warning to 18 million residents of the coast of Peru. We validate the algorithm of the system on recent major earthquakes in other regions, demonstrating its effectiveness and versatility for global deployment.

1 Introduction

Peru is a highly seismic country under the looming hazard of large earthquakes. Analysis of decade-long geodetic time series (1996-2007) along the Central Andes revealed areas of high seismic coupling along the subduction fault (Chlieh et al., 2011). In the central region of Peru, two contiguous 350-km-long asperities, if ruptured together, could trigger an earthquake of moment magnitude (M_w) exceeding 8.5. Further south, near Nazca and Yauca, another seismically coupled area could generate an $M_w \geq 7.5$ earthquake, as the 1913 Arequipa earthquake (M_w 8.2) exemplified. The southernmost coastal regions of Moquegua and Tacna could produce $M_w \geq 8.0$ events, as the 1868 Tacna earthquake (M_w 8.8) showed. Villegas-Lanza et al. (2016) identified similar seismic behaviors in the central and southern regions of Peru by analyzing geodetic data from over 100 sites across the country from 2008 to 2013. This study highlighted significant deformation along Peru's 2,200-km-long margin and identified weak to moderate seismic coupling areas in the northern zone, associated with shallow historical earthquakes (M_w 7.5) in 1953, 1960, and 1996. The study also estimated a large-earthquake recurrence interval of 305 $\pm$ 40 years for the Lima-Callao area, which last broke (M_w 8.8) in 1746.

Consequently, the Peruvian government, including the Instituto Geofísico del Perú (IGP), initiated in 2020 the Peruvian Earthquake Early Warning System (EEWS) project "Sistema de Alerta Sísmica Peruano" (SASPe). This EEWS integrates stations and Regional Operation Centers (COERs) along the Peruvian coast with the aim to provide earthquake alerts to over 18 million inhabitants of coastal communities.

There is a substantial interest among Peruvians in having an EEWS. Indeed, 74% of the respondents to a survey made in Peru (Fallou et al., 2022) declared that they installed The Earthquake Network (Bossu et al., 2022), a smartphone-based EEWS. However, only 22% received the alert message in the application before the 2007 M_w 8.0 Pisco earthquake hit, underscoring the need for an EEWS capable of issuing alert messages earlier. Various EEW algorithms have emerged to address specific scenarios and the unique needs of individual countries. In Peru, the focus of SASPe is on coastal urban areas, which concentrate the largest portion of the national population, and offshore subduction earthquakes, where hypocenters of large earthquakes typically occur at least 50 km from the coast, enabling it to provide warnings without significant blind zones in most locations.

Systems such as ShakeAlert, deployed in California and the US West Coast (Böse et al., 2014), address similar challenges with very short alert times. ShakeAlert employs the τ_c-P_d Onsite algorithm (Böse et al., 2009) and the Earthquake Alarm System (ElarmS) (Brown et al., 2011). The Onsite algorithm utilizes data from the initial 3 seconds recorded by a single station to estimate magnitude and Modified Mercalli Intensity at the station, but does not estimate the location of the earthquake. In contrast, ElarmS analyzes peak displacement and maximum predominant frequency from multiple stations to estimate both the earthquake magnitude and location. ElarmS-3 (Chung et al., 2019), the latest version of ElarmS, uses at least 0.2 seconds of P-wave data recorded by three stations (Ruhl et al., 2019), but integrating data from multiple stations may lead to reduced first alert lead times. Conversely, the pioneer in EEW algorithms, the Urgent Earthquake Detection and Alarm System (UrEDAS), contains a detector and a source characterization estimator (magnitude and location) based on few seconds of P wave recorded by a single station (Nakamura, 1988; Nakamura et al., 2011). Nevertheless, its accuracy differs when applied to regions outside of Japan, such as in California where it tends to overestimate earthquake magnitudes between 3 and 6 based on the initial three seconds of earthquake records (Nakamura & Saita, 2007).

SASPe employs the Ensemble Earthquake Early Warning System (E3WS) algorithm, developed by Lara et al. (2023), to provide timely alerts during subduction earthquakes. E3WS uses data from the initial three seconds of P-wave records at a single three-component station to detect, locate, and estimate the magnitude of earthquakes. This AI-driven algorithm, trained with global data, offers faster and more accurate estimates than existing systems based on single-station data, making it crucial for issuing initial warning messages. Additionally, the algorithm features continuous updates, adjusting the alert radius as the magnitude of the earthquake increases. E3WS's versatility across different geographical regions has been demonstrated in stations in Colombia (Montenegro Folleco, 2023), Japan, Chile, and Peru (Lara et al., 2023). The E3WS detector has also been effectively applied in Haiti to forecast aftershock rates following the 2021 M_w 7.2 Nippes earthquake (Calais et al., 2022).

SASPe enhances Peru's earthquake response capabilities through four strategically designed components. Component 1, Earthquake Knowledge, focuses on seismic research that analyzes earthquake recurrence and risk scenarios. Component 2, Monitoring and Alert, focuses on real-time monitoring through the construction of seismic stations and real-time analysis algorithms that enable the rapid determination of earthquake source parameters for timely public alerts. Component 3, Dissemination and Communication, handles the rapid dissemination of alerts through multiple communication channels. Component 4, Response Capacity, strengthens response strategies by organizing preparedness activities, such as drills and evacuation planning. Collectively, these components integrate scientific research with practical measures, ensuring that both the authorities and the population are well-prepared to respond effectively to seismic events. Components 1 and 2 are managed by IGP, and Components 3 and 4 by Instituto Nacional de Defensa Civil (INDECI, the National Civil Defense Institute).

Here, we present the results of the completed first and second components of SASPe, conducting a comprehensive evaluation of its real-time performance and effectiveness. Our analysis encompasses the development of the SASPe database and the operational framework within the Peruvian Earthquake Early Warning System, with a detailed examination of the alert radius, new algorithmic developments that enhance location accuracy, and evaluation of magnitude estimates. Furthermore, the efficacy of the system under real-time conditions is scrutinized. We also demonstrate the global applicability of the E3WS algorithm, highlighting its adaptability and robust performance in response to various recent major global earthquakes. Finally, our discussion identifies potential blind spots within the system and assesses the lead times provided by SASPe to users for the most critical scenarios.

2 Peruvian EEWS

2.1 Infrastructure and single-station algorithm

SASPe comprises 111 permanent dedicated stations and 10 COERs. The installation started in April 2021 and was finalized in 2023. Inter-station distances range from 20 to 30 km. Each station is equipped with a three-component strong-motion accelerometer, a compact single-board computer (Raspberry Pi 4), and a radio communication system. The latter transmits to the COERs single-station-based alerts and information for multi-station-based alerts. Given the close proximity of potential megathrust earthquakes to at-risk populations, SASPe has adopted for its earliest alerts a single-station-based EEWS approach, and specifically developed the E3WS algorithm (Lara et al., 2023). Leveraging the algorithm's simplicity, we implemented it on the Raspberry Pi 4 at each SASPe station. This setup allows for on-site processing of the EEWS data, enabling the transmission of only the alert signal to the COERs. This approach fosters a lighter, faster, and more resilient communication system.

There is one COER in each of the 10 Peruvian departments located along the coast, managing approximately 11 stations each. COERs will automatically retransmit alert messages to the applications being developed by INDECI via satellite, internet and radio, enabling them to disseminate the alerts to the population. COERs and the strong-motion stations are operational (the first one since April 2021), running the E3WS algorithm and sending alert messages to the COERs, which are then stored on the IGP servers; details of the database are provided in Section 3. The system for transmitting alert messages to the population, comprising sound alarm towers and mobile applications, is still under construction by INDECI.

E3WS processes the accelerometric data through three modules (Fig. 1): a detector, a P-phase picker and a source parameters estimator (Lara et al., 2023). Each station has its own detector model, which was retrained station-by-station following the methodology described by Lara et al. (2023) using specific seismic noise data recorded by each station. For this retraining, we selected 900,000 10-seconds-long windows of noise extracted from 2 weeks of continuous data from each station. The detector distinguishes earthquakes from noise by analyzing a 10-s-long moving window, sliding with a stride of 1 s. The stride is constrained by the seismic data packet transmission period from the digitizer (100 Hz sampling rate) to the Raspberry. If the detector estimates a P-phase probability above 0.8 (a pre-established SASPe detection threshold), the P-phase picker estimates the onset of the P wave within the 10-s triggered time window by employing a 4 s-long moving window, sliding with a stride of 0.2 s. To enhance the precision given by the 0.2-s interval in detecting the onset of the P wave, quadratic interpolation was applied to the probability estimates of the P-phase picking. However, since both the interpolated and original methods yielded similar results in estimating the P arrival time and the hypocenter location, we chose the original method without interpolation. Both methods gave similar results because the uncertainties (mean absolute error) in the P phase picking in the original E3WS are 0.14 seconds, very close to the stride of 0.2 seconds. We set the detection threshold to 0.8 – a relatively high value – to minimize false positives caused by the high noise levels frequently recorded at the stations, to ensure reliable detection of significant earthquakes with $M \geq 4.5$. This high threshold may result in some missed detections of lower magnitude earthquakes ($M < 4.5$), as evidenced by our real-time analyses (see Section 4.1), but these are not significant for SASPe's purposes.

Lastly, the source characterization module estimates the magnitude and the hypocenter location. Its earliest estimate uses the first 3 seconds of records after the P-wave arrival. Following the E3WS configuration recommended by Lara et al. (2023), it uses a window of 10 seconds, including 7 seconds of noise preceding the estimated P arrival time, followed by 3 seconds of P-wave. Continuous updates are executed on progressively longer time windows, extended with a stride of 1 second: the update windows include 7 seconds of noise and N seconds of P wave, with integer N increasing from 4 to 9.

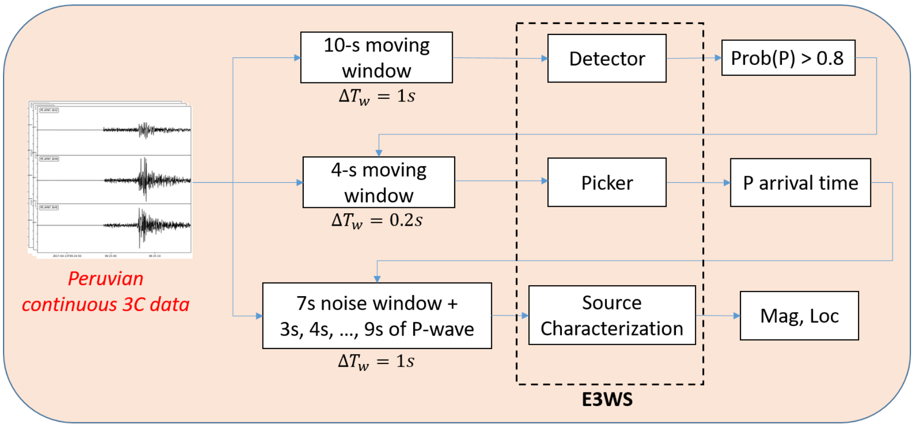

Figure 1. Block diagram of E3WS applied to SASPe. ΔT_w denotes the stride of the moving window.

2.2 Magnitude threshold for alerts

We evaluated acceleration levels along the Peruvian coast using several Ground Motion Prediction Equations (GMPEs), such as Youngs et al. (1997), Atkinson and Boore (2003), Abrahamson et al. (2016), and Zhao et al. (2006). By comparing theoretical accelerations with those observed at SASPe stations, we identified the GMPE by Zhao et al. (2006) as the most suitable for the Peruvian context. We considered synthetic earthquakes across the subduction zone of Peru with depths shallower than 60 km given by the Slab2.0 model (Hayes et al., 2018) at intervals of 0.05 degrees of latitude and longitude, focusing on magnitudes larger than 5. Our analysis revealed small regions in northern Peru (Tumbes and Piura) and southern Peru (Ica and Arequipa) where an M 5.8 earthquake could reach accelerations of 10% g, a threshold considered capable of causing minor damage to the abundant precarious housing. However, we observed that only M $\geq$ 6 earthquakes could generate accelerations greater than 10% g across the entire Peruvian coast. Moreover, records from SASPe stations and the National Seismic Network of Peru confirmed no M $<$ 6 earthquake produced a Peak Ground Acceleration (PGA) exceeding 10% g.

Furthermore, we estimated ground acceleration levels along the central coast of Peru, including Lima, home to nearly a third of the nation's population (11 millions). We applied the methodology of Pulido et al. (2015), which incorporates both synthetic and real earthquake data. This analysis considered $5 \leq$ M ≤ 6.5 earthquakes located offshore west of Callao with the following combinations of hypocentral depth and epicentral distance to Callao: (40 km, 60 km), (50 km, 40 km) and (60 km, 50 km). We found that an earthquake 50 km deep and 40 km away from the coast can generate ground accelerations exceeding 10% g only if M $\geq$ 6. The other two scenarios, with depth-distance combinations of (40 km, 60 km) and (60 km, 50 km), resulted in PGAs of 7.8% g and 9.2% g, respectively, for M = 6. Consequently, SASPe COERs initiate an alert message if the event magnitude exceeds 6.

2.3 Alert radius and its tolerance

Warnings are intended to be sent to users within a certain distance to the epicenter, denoted as the "alert radius". The alert radius is defined by a threshold on estimated PGA of 5% g. This threshold was selected to be more conservative compared to the 10% g that could potentially endanger substandard housing. The PGA is estimated by using the source parameters provided by E3WS and the GMPE by Zhao et al. (2006). The GMPE is a function f relating PGA to epicentral distance r, hypocenter depth Z and magnitude M:

$$PGA = f(r, Z, M). \tag{1}$$

The alert radius $R(Z, M)$ is defined as the distance from the epicenter (X, Y) that satisfies

$$f(R, Z, M) = 0.05\,g. \tag{2}$$

To accelerate calculations, SASPe stores in the COERs a table of pre-computed alert radii for the relevant range of Z and M, with depth precision of 1 km and magnitude precision of 0.1 unit.

We add a tolerance to the estimated alert radius to account for uncertainties in the estimates of epicenter location, hypocentral depth and magnitude. The rationale to determine the tolerance value is as follows. Taking the partial derivatives of the defining equation 2, we get the following relation between perturbations of alert radius (dR), event magnitude (dM) and depth (dZ):

$$(\partial f/\partial r)dR + (\partial f/\partial M)dM + (\partial f/\partial Z)dZ = 0 \tag{3}$$

Thus, an uncertainty dM in the magnitude estimate and dZ in the depth estimate leads to an uncertainty in alert radius of:

$$dR = -\left[(\partial f/\partial M)dM + (\partial f/\partial Z)dZ\right]/(\partial f/\partial r). \tag{4}$$

This uncertainty dR is a function of Z and M; note that the partial derivatives involved are evaluated at $r = R(Z, M)$. The position of the alert circle is also affected by the uncertainties in epicenter location (dX and dY), leading to the following total uncertainty in alert radius:

$$\Delta R(Z, M) = \sqrt{dX^2 + dY^2} + |dR|(Z, M) \tag{5}$$

We define the tolerance on the alert radius as the maximum of ΔR among all values of Z and M within the ranges of interest.

We computed the contributions to alert radius uncertainties from errors in location ($\sqrt{dX^2 + dY^2}$), magnitude ($dR_M(M, Z)$), and depth ($dR_Z(M, Z)$) using a single station and the first 3 seconds of P wave (Fig. 2). $dR_M(M, Z)$ and $dR_Z(M, Z)$ represent the first and second terms of equation 4, respectively. Location errors were computed based on location residuals obtained from SASPe data. For uncertainties related to magnitude and depth uncertainties, we apply the GMPE by Zhao et al. (2006) for M $\geq$ 6 earthquakes to obtain $(\partial f/\partial M)$, $(\partial f/\partial Z)$, $(\partial f/\partial r)$, and the residuals in magnitude and depth using SASPe data for earthquakes with depths between 20 and 60 km, yielding dM and dZ. Our analysis, based on a 3-second P-wave windows, indicates that for M 6 earthquakes, alert radius uncertainties associated with location errors exceed the combined uncertainties due to magnitude and depth errors, and are similar to the combined uncertainties for M 7 earthquakes. Moreover, the alert radius uncertainties due to location errors are larger than uncertainties due to magnitude or depth errors for all M $\geq$ 6 earthquakes. This finding underscores the need to enhance location estimates to more accurately estimate the alert radius.

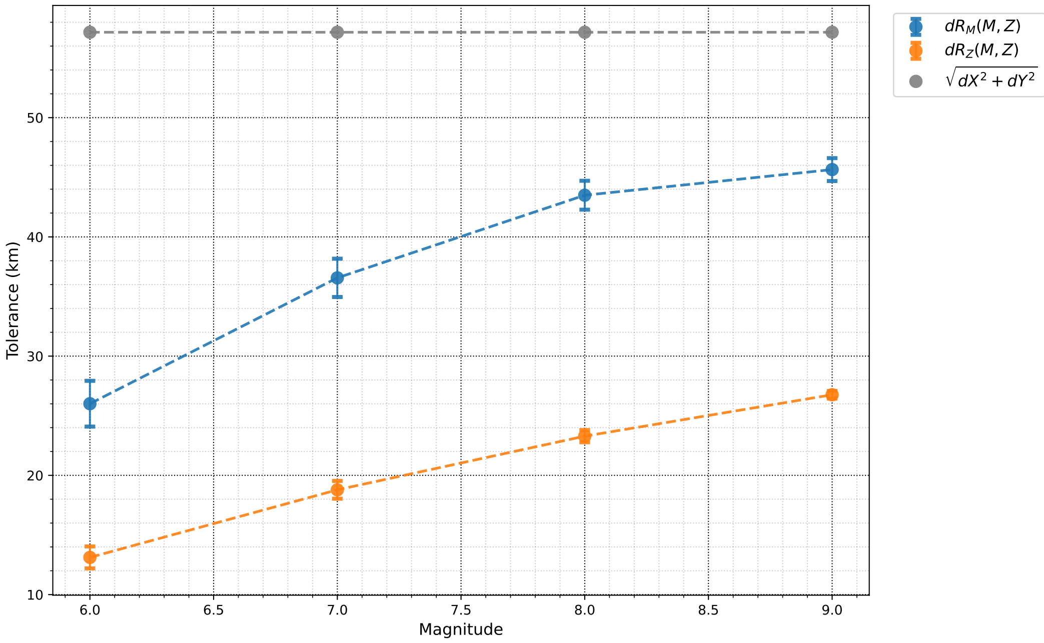

Figure 2. Contributions to alert radius uncertainities from errors in location ($\sqrt{dX^2+dY^2}$), magnitude ($dR_M(M,Z)$), and depth ($dR_Z(M,Z)$), based on a single station and the first 3 seconds of the P-wave for $M \geq 6$ earthquakes with depths Z from 20 to 60 km. Circles represent the mean of the alert radius uncertainties among all values of Z, and bars indicate their standard deviation.

2.4 Improvement in location estimates

The largest errors in the location estimates provided by the original E3WS algorithm come from errors in the estimates of the back-azimuth derived from three-component data recorded by a single station (Lara et al., 2023). Back-azimuth residuals decrease as magnitude increases (Fig. 3a). Acceptable estimates (errors less than 20°) are generally associated with a high signal-to-noise ratio (SNR) and with high linearity of signal polarization. The latter is quantified by the ratio of the maximum eigenvalue of the three-component signal covariance matrix to the remaining two eigenvalues (Fig. 3b), which we denote hereafter as the eigenvalue ratio. High SNR, typically owing to large magnitude, reduces artifacts caused by background noise in the covariance matrix estimation, leading to more accurate estimation of the eigenvalues. Even at equal SNR, two earthquakes might have different degrees of signal linearity, due for instance to different degrees of wave scattering. This is exemplified in Fig. 3a,c, where the M 6.7 earthquake exhibits higher eigenvalue ratio than the M 8 earthquake, resulting in better back-azimuth estimates. The M 6.7 earthquake being deeper (67 km) than the M 8 earthquake (39 km), it is expected to have less scattering on the source side, which promotes a clearer, more linear P wave.

To address limitations in location estimation from a single station, we extend E3WS to use multiple stations. Specifically, we investigate scenarios where the P-wave has been detected by several stations at the time when the nearest station has recorded 3 seconds of the P-wave, which is the time of the first alert in SASPe. Computing theoretical P arrival times at each SASPe station for M $\geq$ 6 earthquakes in Peru since 1970, we found that typically 3 to 4 stations capture the P-wave within 3 seconds following the P-wave

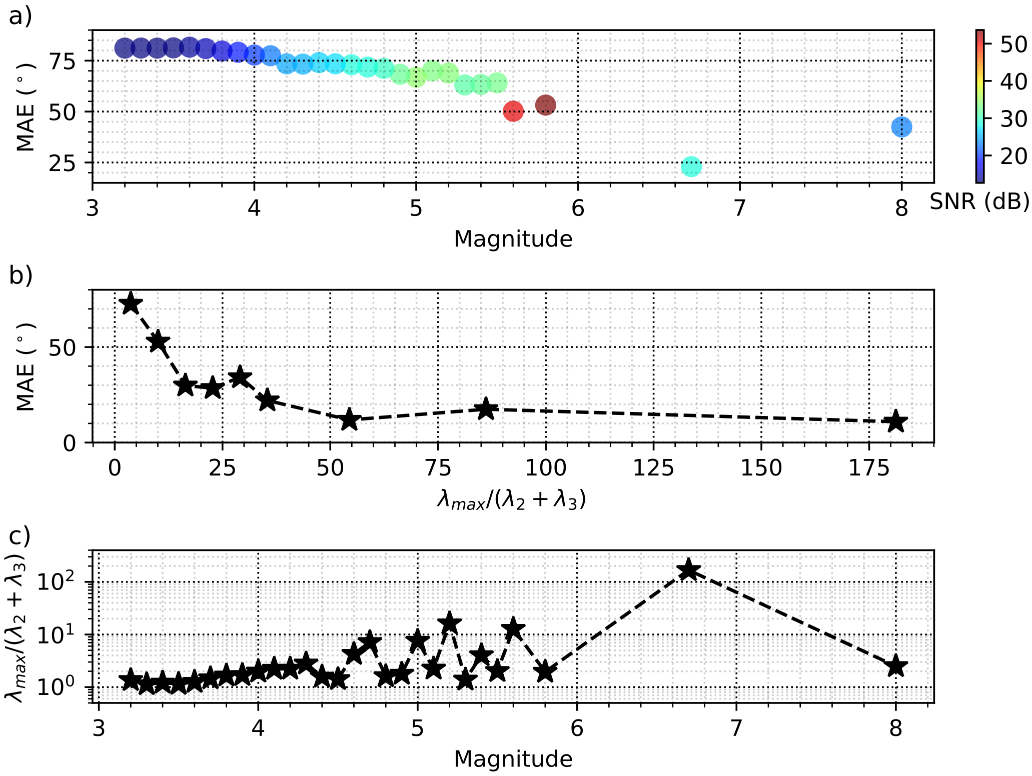

Figure 3. Errors back-azimuth estimates and analysis of eigenvalues conducted using data from the National Accelerometer Network of Peru since 2015. Publicly available data can be downloaded from `www.igp.gob.pe/servicios/aceldat-peru/`. Mean Absolute Error (MAE) in the back-azimuth estimates as a function of (a) magnitude (colors indicate the signal to noise ration (SNR)) and (b) eigenvalue ratio. c) Distribution of eigenvalue ratios as a function of magnitude.

arrival at the nearest station (Fig. S1). Consequently, leveraging data from multiple stations presents an opportunity to enhance location estimation accuracy.

2.4.1 One station

For cases where only one station is available within 3 seconds of the first P-wave arrival, we examined the potential benefits of using P-wave windows shorter than 3 seconds for back-azimuth estimation (e.g. Noda et al. (2012)). We found that the lowest errors are achieved within the first 0.5 seconds of the P wave (Fig. S2). Therefore, in the updated E3WS we estimate the back-azimuth using P wave windows of 0.1, 0.2, 0.3, 0.4, and 0.5 seconds, selecting the window that offers the highest eigenvalue ratio. This approach replaces the use of 3-seconds windows for back-azimuth estimation of the original E3WS.

2.4.2 Two stations

Once the second station has recorded 0.5 s of P wave (Fig. 4b), we update the earthquake location as follows:

a. Given the distance and depth estimated by E3WS based on the first station (d_1, z_1), we estimate the P-wave travel time from the hypocenter to station 1 (t_{p_1}) using theoretical travel times: $t_{p_1} = t(d_1, z_1)$.
b. We calculate the earthquake origin time (t_o) as the P-wave arrival time picked by E3WS at station 1 (P_1) minus t_{p_1}.
c. We compute the P-wave velocity (v_p) as d_1/t_{p_1}.
d. Given the P-wave arrival time picked by E3WS at station 2 (P_2), we estimate the epicentral distance to station 2 as $d_2 = v_p \times (P_2 - to)$.
e. Based on the positions of the stations (x_1, y_1) and (x_2, y_2), we determine the two possible epicenters (x_{p_1}, y_{p_1}) and (x_{p_2}, y_{p_2}) at the intersections between the circle of radius d_1 centered at station 1 and the circle of radius d_2 centered at station 2.
f. For each station, we estimate the back-azimuth using 0.1, 0.2, 0.3, 0.4 and 0.5 s of P-wave, and choose the estimate that has the highest eigenvalue ratio.
g. For each station, based on the distance and back-azimuth estimates, we estimate an epicenter. Then, we average both epicenters to obtain (x_e, y_e) (black star in Fig. 4b).
h. Finally, we calculate the distance from (x_{p_1}, y_{p_1}) to (x_e, y_e) and from (x_{p_2}, y_{p_2}) to (x_e, y_e). The one with the smaller distance is the estimated epicenter.

For steps c and d, we attempted to use pre-computed tables containing travel times as a function of distance and depth. However, the results showed slight degradation, leading us to retain the simple approach described above.

2.4.3 Three stations or more

When data is available from 3 stations or more (Fig. 4c and 4d), we estimate the epicentral distance at the "i" station as $d_i = (P_i - to) \times v_p$. Then, based on the station locations (x_i, y_i) and estimated distances d_i, we estimate the epicenter location by triangulation using the least squares method with Cauchy loss function.

Using multiple stations is feasible due to the precision of the first estimate, which relies on 3 seconds of P wave recorded by a single station. This estimate serves as the basis for estimating epicentral distances at other stations. Therefore, we can leverage multiple stations without waiting for each station to have 3 seconds of records after the P-wave arrival. Instead, we only require 3 seconds from the first station and 0.5 seconds from the remaining stations. 3 seconds after the P-wave arrival at the nearest station, on average 3 to 4 stations have captured a P wave (Fig. S1) and ∼3 stations have recorded over 0.5 seconds of P wave. These stations contribute to improve the location estimation.

3 Database

We compile a database of seismic waveforms sourced from SASPe stations, covering the operational period of the first station from April 2021 to July 2023. Based on the United States Geological Survey (USGS) earthquake catalog (`https://earthquake.usgs.gov`), M $\geq$ 6 events in Peru since 1970 exhibit a mean depth of 40 km, with standard deviation (STD) of 20 km, and are located within an average distance from the nearest SASPe station of 35 km with STD of 30 km. Hence, we filter the database to exclude observations with epicentral distances longer than 100 km and events deeper than 100 km. The database contains 6,054 seismic waveforms from 1,973 M $\geq$ 3 earthquakes (Fig. 5). The largest event is an M 6.8 earthquake that occurred on March 18, 2023 in the South of Ecuador.

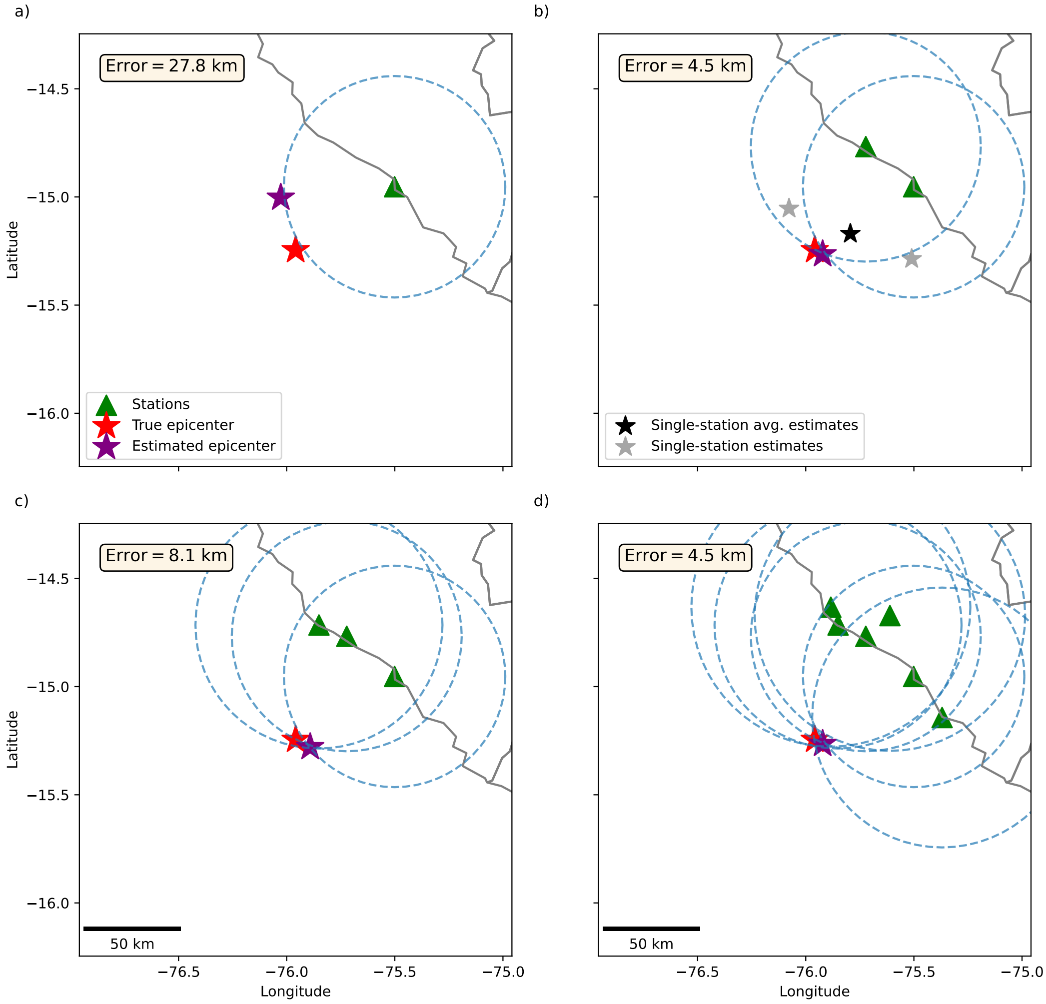

Figure 4. Estimation of the earthquake location based on a single station (a), 2 stations (b), 3 stations (c) and more than 3 stations (d).

4 Results

We present the performance of the E3WS algorithm as the core algorithm of the Peruvian EEWS, SASPe. We first show the results of earthquake detection, magnitude estimation, and location estimation. We then assess the tolerance in the alert radius. Next, we provide an illustrative example of the performance of SASPe in a real-time scenario during the M 5.4 Lima earthquake of February 15, 2024. Finally, we evaluate the performance of the E3WS algorithm during recent significant earthquakes worldwide.

4.1 Detection

The performance of the E3WS detection algorithm during the over 2-year analysis period is reported in Table 1. Statistics are provided for false negatives (missed events) and false positives.

SASPe misclassified 795 earthquakes as noise (false negatives). Among these earthquakes, 99.6% have M $\leq$ 4.0 and a mean hypocentral distance to the nearest station of 80 km. The remaining 0.4% of the missed earthquakes are M $\leq$ 4.5 events, and their clos-

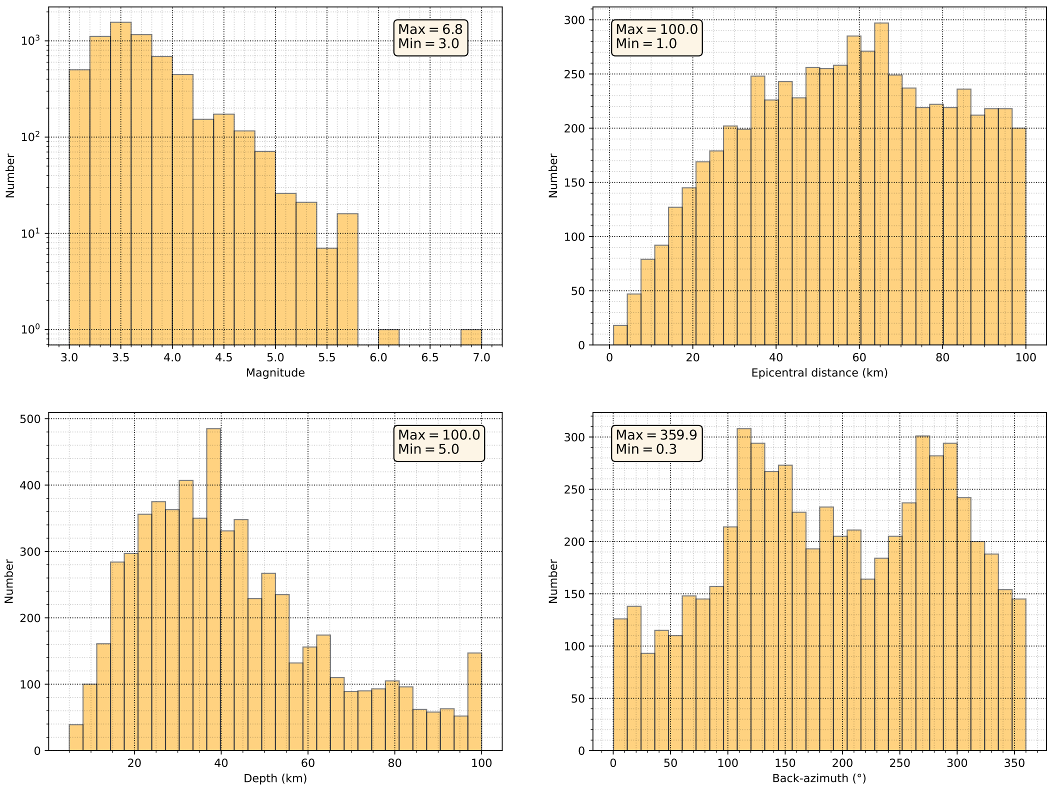

Figure 5. Magnitude, epicentral distance, depth and back-azimuth distributions of the SASPe database.

est station is approximately 100 km away. False negatives arise from SASPe's elevated detection trigger threshold set at 0.8, which reflects the emphasis on identifying potentially hazardous earthquakes. False negatives are caused by signals with low signal-to-noise ratio associated to events that do not cause damage.

False positives (noise misclassified as earthquakes) in SASPe primarily stem from impulsive noise generated by people or external agents, such as animals or industrial activities. Using all stations independently, we identified 728 false positives. They are associated to estimated magnitudes centered around 3.6, with a maximum magnitude of 4.5. None of the false positives exceed the SASPe magnitude threshold of 6 for issuing alert messages.

4.2 Source characterization

The magnitudes estimated on SASPe data, based on 3 seconds of P wave recorded by the nearest station to the earthquake epicenter, are shown in Fig. 6b. The resulting performance is consistent with the performance on global data (Lara et al., 2023). All M $<$ 6 earthquakes are correctly estimated as M $<$ 6. Given SASPe's threshold of M $\geq$ 6 for broadcasting alert messages, this result implies that no false alerts are generated. For the two events for which SASPe estimates M $\geq$ 6, an M 6.1 and an M 6.8 earthquake, the magnitude estimates based on 3 seconds of P-wave data are 6.4 and 6.3, respectively. In both instances, the alert message is promptly issued, with no false negatives. There is a slight tendency for overestimation around M 3, as observed on other datasets (Lara et al., 2023), but this is inconsequential for SASPe purposes. Magnitude estimates obtained at each station independently based on 3 seconds of P wave (Fig. 6b) have a con-

Table 1. False Negatives and False Positives of the E3WS earthquake detection algorithm in over 2 years of continuous SASPe data. For false negatives, we report real magnitude, nearest station distance (mean ± STD km), and number of events. For false positives, we report E3WS magnitude estimates and number of events.

False negatives			**False positives**	
M_{true}	Nearest hyp. (km)	Instances	M_{E3WS}	Instances
3.0	74.6 ± 19.7	102	3.0	8
3.1	78.3 ± 19.8	122	3.1	18
3.2	74.3 ± 18.5	126	3.2	53
3.3	79.4 ± 19.2	119	3.3	76
3.4	81.2 ± 19.2	115	3.4	91
3.5	80.6 ± 23.6	75	3.5	134
3.6	78.0 ± 16.9	50	3.6	128
3.7	81.7 ± 17.8	44	3.7	78
3.8	83.4 ± 18.7	22	3.8	46
3.9	84.1 ± 21.1	10	3.9	40
4.0	69.9 ± 13.2	7	4.0	19
4.1	89.5	1	4.1	21
4.2	98.1	1	4.2	10
4.3	−−	0	4.3	9
4.4	−−	0	4.4	3
4.5	105.5	1	4.5	4

sistent performance, which instills confidence in utilizing a different station than the one closest to the source in case the latter is not operational.

The epicentral residuals for the single-station and mutiple-station methods described in Section 2.4 are shown in Fig. 7. In Fig. 7a, we show the average residuals and their 95% confidence interval (CI). The latter is estimated through bootstrapping, as outlined by Dutilleul et al. (2024). To do so, we create 1000 bootstrap samples by randomly drawing data points from the original dataset, we calculate the mean for each of these bootstrap samples, and then determine the range between the 2.5th and 97.5th percentiles from these sorted means. In Fig. 7b, we show the residual distributions in more detail through boxplots.

The accuracy of location estimates improves when using multiple stations. The residual averages decrease from 57 km based on a single station to 41 km based on multiple stations, a 28 % improvement depicted in Fig. 2, which sharpens the precision of the initial alert radius. For M 6 earthquakes, the difference between distance-based and magnitude-based tolerances decreases from 31 km (single station) to 15 km (multiple stations), and from 21 km (single station) to 5 km (multiple stations) for M 7 earthquakes. This indicates that while errors in epicentral distances continue to influence tolerances, their impact is now less pronounced compared to magnitude errors. Moreover, for M $\geq$ 7.7 earthquakes, the impact of errors in magnitude estimates – derived from the initial 3 seconds of P-wave data – becomes more significant, differing from earlier observations where epicentral distance errors predominantly influenced alert radius tolerances across all M $\geq$ 6 earthquakes. This results in an improved estimate of alert radius for the first alert. In subsequent updates, the epicentral residuals remain similar up to 6 s after the P wave arrival at the first station. At later times, the location errors improve more and faster

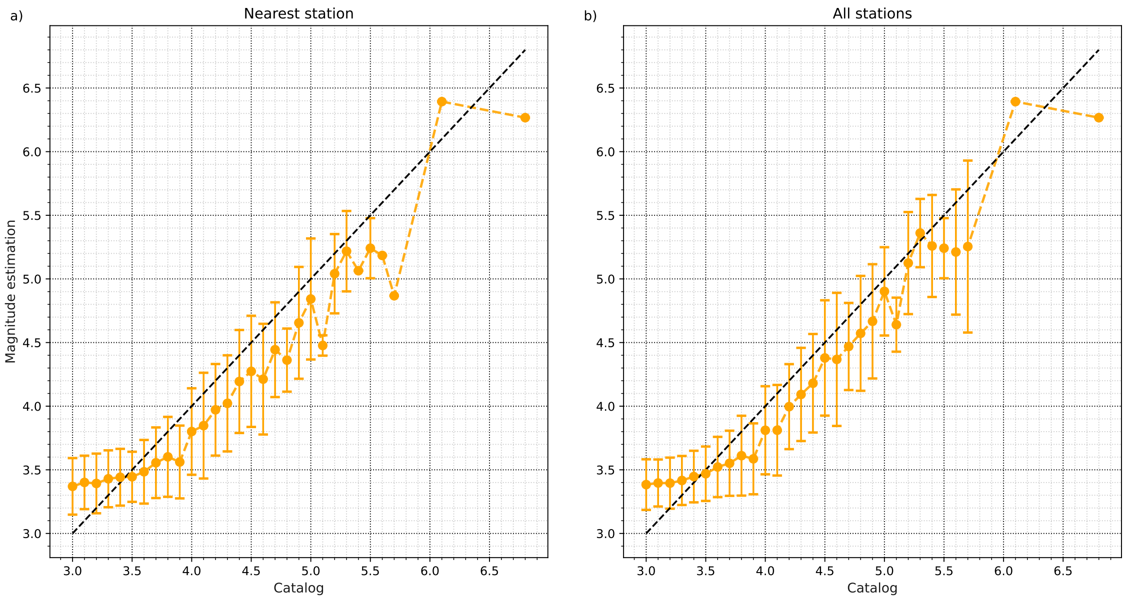

Figure 6. E3WS magnitude estimates based on 3 s of P wave recordings (a) at the nearest station to the seismic source and (b) at all stations within 200 km from the source. Each circle represents the mean of the bin estimates, and the bars the STD. The black dotted line indicates an ideal estimate.

when using multiple stations than when using a single station: average errors at 7 s are 38 km for multiple stations and 56 km for a single station, and at 10 s they are 31 km and 53 km, respectively.

The use of multiple stations not only improves location estimates but also reduces outliers (Fig. 7b). The median errors and the interquartile range remain similar using 3, 4, 5 and 6 s of earthquake data from the nearest station. For a single station, the median error is approximately 47 km (Q1: 31 km, Q3: 68 km). With multiple stations, the median error is 35 km (Q1: 20 km, Q3: 58 km), with fewer outliers compared to a single station. For this reason, the median of the residuals using P wave windows longer than 6 seconds converges to the average of the residuals, as they contain a smaller number of outliers. Conversely, for the initial estimate (3 seconds of P wave), the median (35 km) is smaller than the average of the residuals (41 km). For longer windows, the median errors decrease from 31 km to 30 km using 7 and 10 s of P-wave records at the nearest station, respectively. Furthermore, the interquartile range decreases linearly, and the number of outliers tends to diminish.

4.3 Alert radius

We illustrate in Fig. 8a the theoretical alert radius based on GMPEs with hypocentral depth of 40 km and the additional tolerances. We also present the evolution of tolerances derived from 3 seconds of P-wave recorded at the nearest station, based on continuous updates in magnitude and depth provided by E3WS, along with its improved localization based on the multi-station workflow of Section 2.4.

For a magnitude 6 earthquake, the theoretical alert radius is 89 km (Fig. 8a). The tolerance necessary to compensate for errors in the initial E3WS estimate (3 s of P-wave at the nearest station) is 82 km (Fig. 8b). Therefore, the total alert radius broadcast

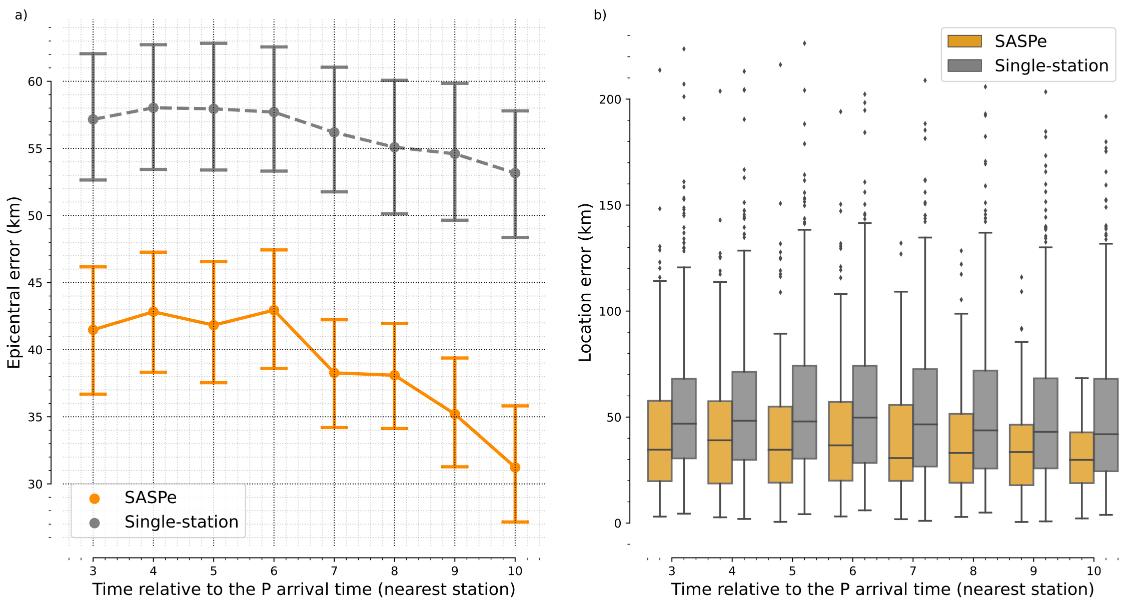

Figure 7. (a) Average location residuals and confidence intervals using a single station (grey) and all available stations (orange) 3 to 10 s after the P-wave arrival on the nearest station. (b) Median residuals and interquartile range in a boxplot. The boxes span from the first quartile (Q1, 25% of the data) to the third quartile (Q3, 75% of the data). The horizontal line inside the boxes represents the median. Vertical lines outside the boxes extend to 1.5 times the interquartile range (Q3−Q1). Outliers, represented by dots, fall beyond this range.

by SASPe is 171 km. Continuous updates contribute to refine the estimation of magnitude and location, thereby improving tolerances. For the same example, the tolerance based on 5 s, 7 s and 10 s of P-wave is 79 km, 76 km and 71 km, respectively, leading to an update of the alert radius to 168 km, 165 km and 160 km, respectively.

Alert radius tolerances based on 3 s recorded at the nearest station are primarily influenced by epicenter location errors, constituting 42% of the total error, followed by 33% attributed to errors in magnitude and 25% to errors in depth. We show the dependence on alert radius tolerances for larger windows in Fig. S3.

4.4 SASPe performance in real time

We present the performance of SASPe during the M 5.4 earthquake of February 15, 2024 (Fig. 9). Although the event did not reach a magnitude larger than 6, which is required to activate an official alert, IGP simulates alert messages for M $\geq$ 5 earthquakes as part of its testing protocol. This involves storing the estimated magnitude and hypocenter, and calculating the alert radius. Additionally, an audible alarm is activated at the Centro Sismológico Nacional (CENSIS) located at the IGP facilities in Lima, and the simulated alert message is simultaneously sent to the COER and stored on the IGP servers. This event is a compelling example to illustrate the functionality of SASPe because of its proximity to Lima, the capital and most populated area of the country. We show the SASPe performance for the two recorded M $\geq$ 6 earthquakes in the supplementary information (Fig. S4 and S5).

The earthquake occurred on the Peruvian subduction fault at a depth of 57 km, as reported by IGP. E3WS detected the earthquake using seismic records from the near-

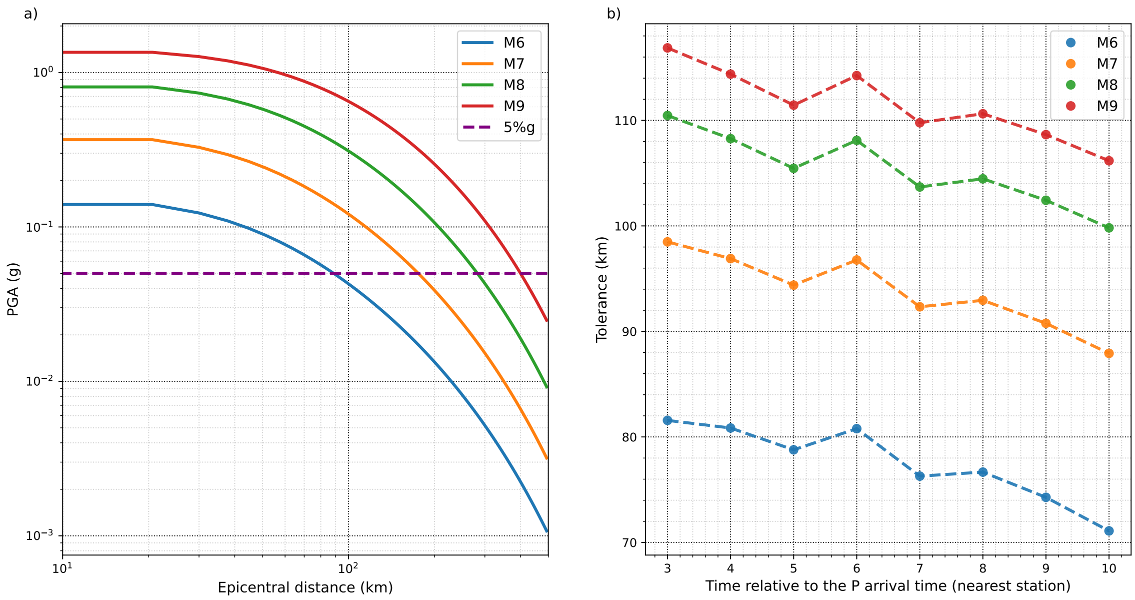

Figure 8. (a) Theoretical alert radius based on the GMPE by Zhao et al. (2006) for M $\geq$ 6 earthquakes with hypocentral depth of 40 km. Purple dotted line represents the 5% g acceleration threshold in the SASPe alert radius. (b) Tolerances in the alert radius as a function of time relative to the P-wave arrival time at the nearest station for M $\geq$ 6 earthquakes.

est station (SFRN). It estimated the P wave arrival time at 10.7 seconds after the earthquake origin time. The first magnitude estimate, using the first 3 s of the P wave, was 5.2. This information was sent to the COER and IGP. The magnitude was below the M 6 threshold to issue an official alert.

We calculated the user lead time as the difference between the S wave arrival time at the station and the arrival of the first simulated alert message at the COERs and IGP. Lead times ranged from 3.1 s around the SFRN station (located 20 km from the epicenter) to 28 s at the SASPe-issued alert radius limits. In the center of Lima, the most densely populated area, lead times ranged from 9 to 21 seconds.

The theoretical alert radius covers two SASPe stations with records exceeding 5%g. However, records from one SASPe station and two stations from the National Seismic Network of Peru that exceed 5%g are outside of the theoretical alert radius. In contrast, the theoretical alert radius plus its tolerance includes all the stations where accelerations exceeding 5%g were recorded, reflecting a conservative approach aimed at covering all areas experiencing significant accelerations. This is particularly important in densely populated regions such as Lima, which is home to over 11 million people (Instituto Nacional de Estadística e Informática, INEI, `https://www.gob.pe/inei/`). Furthermore, all stations recorded PGAs below 10% g (risky for precarious housing), supporting our decision to establish a magnitude threshold of 6 for issuing an official alert, as detailed in Section 2.2.

4.5 E3WS around the world

We assess the performance of the E3WS algorithm for major earthquakes that occurred in 2023 and 2024 worldwide (Table 2) to showcase the portability of the algorithm. We simulate the real-time processing and adhere to the same criteria for disseminating

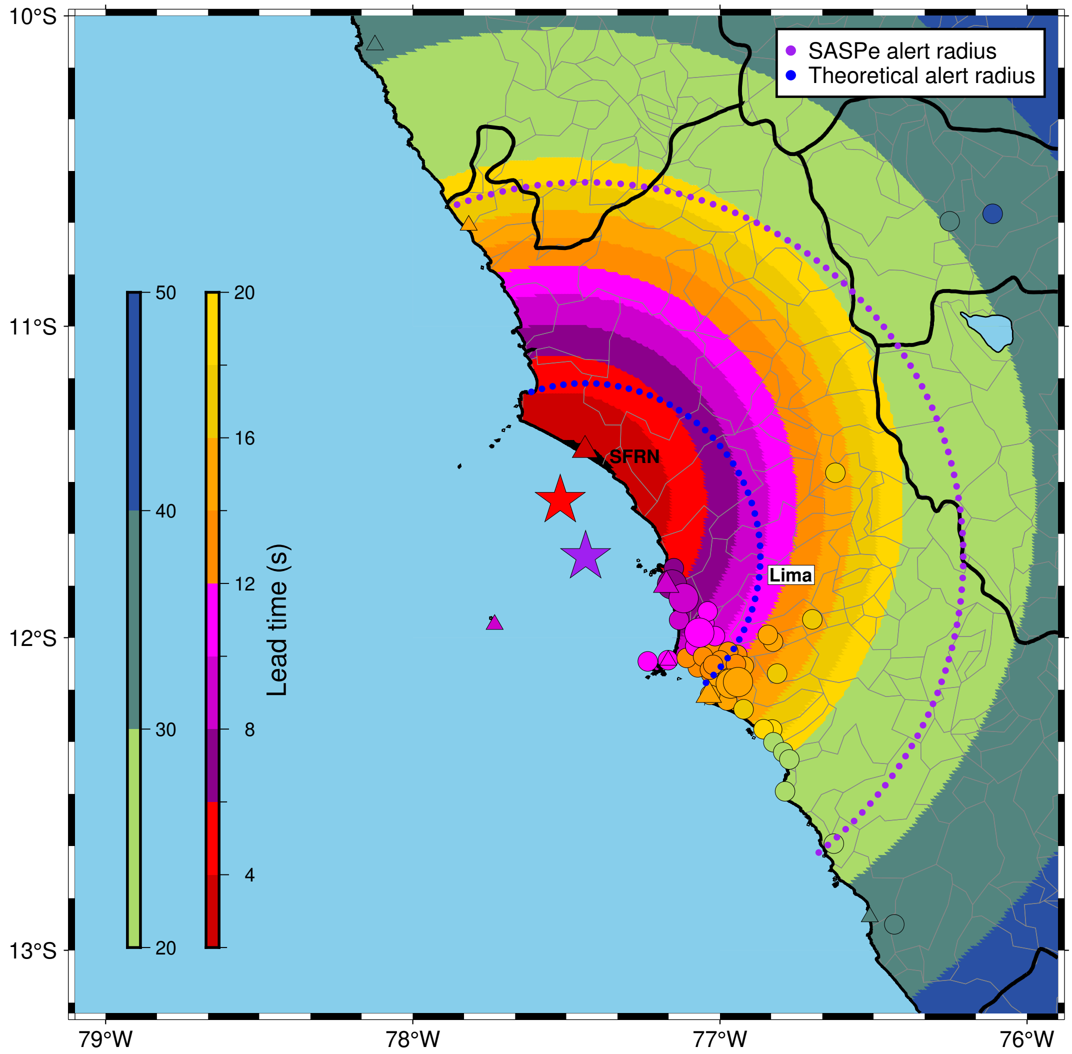

Figure 9. SASPe performance during the M 5.4 earthquake in Lima on February 15, 2024, based on the first estimate (3 seconds of records at the nearest station - SFRN). SASPe stations are depicted as triangles, while stations of the National Seismic Network of Peru are represented by circles. Larger triangles/circles indicate stations with PGA values exceeding 5%g. User lead times are color-coded based on the color bar. Theoretical alert radius and SASPe-issued alert radius are shown in blue and purple circles, respectively. The background coloring represents theoretical user lead times: theoretical S-wave arrival times minus the time it took for the E3WS to issue the alert. The color within the triangles and circles indicates actual user lead times: S-wave arrival times observed on the seismograms minus the alert issuance time by E3WS. The red star denotes the true epicenter, while the purple star represents the estimated epicenter.

the alert message as prescribed by SASPe (M $\geq$ 6 trigger threshold to issue alarms). In all instances, the actual magnitude (from USGS) exceeds 6, and the E3WS magnitude estimate based on the first 3 s of data from the station nearest to the source also indicates M $\geq$ 6. Furthermore, these estimates persist as M $\geq$ 6 for longer windows. In some cases, it is possible to estimate the final earthquake magnitude using 9 seconds of the P wave at the closest station, as observed in the 2023 M 6.8 Marrakech earthquake in Morocco. Notably, E3WS demonstrates its capability to provide accurate estimates even with saturated seismograms, such as those observed at SDPT and TIO stations, which are broadband sensor stations nearest to the 2023 Alaska and Morocco earthquakes, respectively.

We compute the user lead time provided by E3WS as the difference between the arrival time of the S wave and the time E3WS identifies that the magnitude exceeds 6. In all cases, the user lead time around the location with the greatest loss of life (excluding Alaska, where there were no fatalities) is positive. Time provided to the user ranges from 0.2 seconds for the 2023 Marrakech earthquake to 13.7 seconds for the Alaska earthquake in 2023, and extends to 30 seconds for the 2024 Noto earthquake in cities that reported human losses. The lead time in Marrakech is short (0.2 s) because this city is closer to the epicenter than the nearest station to the epicenter (TIO), highlighting the importance of having a station as close to the source as possible in an EEWS. For users near the TIO station, E3WS provides 10 s of lead time.

In the case of the January 1st 2024 Noto earthquake, we computed the user lead times as the difference between the time when E3WS identified an M $\geq$ 6 earthquake and the time at which ground acceleration reached 5% g, to provide a more practical metric, leveraging the high density of ground motion recordings in Japan. The Japan Meteorological Agency (JMA) cataloged two sub-events during this earthquake: a M 5.9 at 07:10:09.5 UTC and a M 7.6 at 07:10:22.6. As both sub-events were very close in time, only 12 s apart, E3WS detected and estimated the magnitude of the first sub-event as M $\geq$ 6 at 3.4 s after the earthquake origin time. This rapid response is a result of the very short distance between the station and the seismic source. For users in the city of Suzu, which experienced the highest number of human losses (103), the alert would arrive 2.2 s before the earthquake shaking exceeded 5% g. For neighboring cities such as Wajima, where there was a significant number of human losses (102), the E3WS algorithm would have generated 11 s of lead time. Furthermore, for more remote cities with fatalities such as Anamizu, Nanao, Shika and Hakui, E3WS would have provided 13.4, 19.3, 30, and 15 seconds of lead time, respectively.

Table 2. User lead times for major earthquakes in 2023 and 2024. Columns detail the earthquake name, closest E3WS station, actual magnitude, E3WS estimated magnitudes at 3 s and 9 s, and user lead time in cities which endured fatalities. For the Noto earthquake the lead time is defined relative to the time when recorded ground accelerations exceeded 5% g at each city. For the other events it is relative to the S-wave arrival time.

Earthquake	Station (km)	M_{true}	$M_{E3WS_{3s,9s}}$	User lead time
2023 Guayas, Ecuador	ACH2 (53 km)	6.8	6.4, 6.4	Guayaquil (7.3 s)
2023 Turkey mainshock	4615 (21 km)	7.8	6.6, 6.8	Kahramanmaraş (5.3 s)
2023 Turkey aftershock	4631 (21 km)	7.5	6.6, 6.4	Kahramanmaraş (10.1 s)
2023 Alaska, USA	SDPT (108 km)	7.2	6.3, 6.6	King Cove (13.7 s)
2023 Marrakech, Morocco	TIO (108 km)	6.8	6.7, 6.8	Marrakech (0.2 s) Ouarzazate (10.0 s)
2024 Noto, Japan	ISKH01 (4 km)	7.5	6.4, 7.1	Suzu (2.2 s) Wajima (11 s) Anamizu (13.4 s) Nanao (19.3 s) Shika (30 s) Hakui (15 s)

5 Discussion

5.1 Lead times for nearby megathrust earthquakes

We evaluate user lead times for earthquakes along the Peruvian subduction megathrust using simulated earthquake scenarios. We consider synthetic sources on a 0.05°-spacing grid (in both latitude and longitude), with depths shallower than 60 km, along the Peruvian subduction megathrust using the slab geometry given by the Slab2 model (Hayes et al., 2018). We consider another 0.05°-spacing grid along the coastal region of Peru (receiver grid) to calculate theoretical lead times for earthquakes within 100 km of epicentral distance from each receiver location. We compute the user lead time by subtracting 3 s (E3WS first estimate delay) from the difference between the S-wave arrival time at the analyzed location and the P-wave arrival time at the nearest SASPe station. For each point on the receiver grid, we calculate the average user lead times (Fig. 10a) and their STD (Fig. 10b).

Our analysis reveals that SASPe typically provides user lead times ranging from 9 to 11 seconds for residents near the Peruvian coast, where the epicentral distance is between 62 km and 73 km. In Tumbes and specific areas of Piura, however, the lead times slightly decrease, ranging from 7 to 9 seconds for epicentral distances between 54 km and 64 km. For communities further inland, where epicentral distances span from 73 km to 83 km, lead times consistently remain between 11 and 13 seconds. In more isolated regions, where distances exceed 94 km, lead times extend beyond 15 seconds.

The STD of lead times ranges from 2 to 4 seconds near the coast in central Peru and the departments of Ica and northern Arequipa. In northern Peru, STDs vary from 4 to 7 seconds, while in southern Arequipa and the southernmost departments, they range from 4 to 6 seconds. For the more remote areas with epicentral distances exceeding 85 km, the STDs range between 0 and 2 seconds.

Furthermore, we calculated user lead times for two historical earthquakes that occurred approximately 60 km offshore of Lima on October 3, 1974 (M 7.7), and November 9, 1974 (M 7.2). Using theoretical travel times, we estimate that SASPe would have provided mean $\pm$ STD lead times of 12.6 $\pm$ 3.2 seconds for the M7.7 earthquake and 12.1 $\pm$ 2.2 seconds for the M7.2 earthquake for locations 100 km away from the epicenter. These results are consistent with those depicted in Fig. 10 and validate the effectiveness of SASPe in providing, typically, timely alerts.

5.2 Blind spots

We assess the existence of blind spots in Peru, where SASPe fails to provide positive user lead time, indicating locations where the S-wave has already arrived by the time SASPe broadcasts the alert message. Considering SASPe's purpose to monitor potentially hazardous earthquakes on the subduction fault, we consider the same grid of sources and receivers as in Section 5.1. For each location on the grid of receivers, we select the earthquake from the grid of sources whose S-wave has the shortest source-site travel time.

The analysis reveals that all 10 departments along the Peruvian coast can exhibit positive user lead times, typically ranging from 0 to 10 or 20 seconds for the most critical cases (Fig. 11). In the departments of Piura, Lambayeque and Ica, earthquakes originating in specific locations can result in negative lead times at some locations, but the alert remains useful away from these specific locations. Note that the map shows the worst-case scenario for each location.

We also computed the lead times for very large earthquakes (M $\geq$ 7 shallower than 100 km) that occurred in Peru since 1970. In 88% of the cases, we observe positive lead times, primarily falling between 0 and 15 seconds. Some events have minimum alert times between 0 and 5 seconds, for instance the M 8 2007 Pisco earthquake (department of Ica)

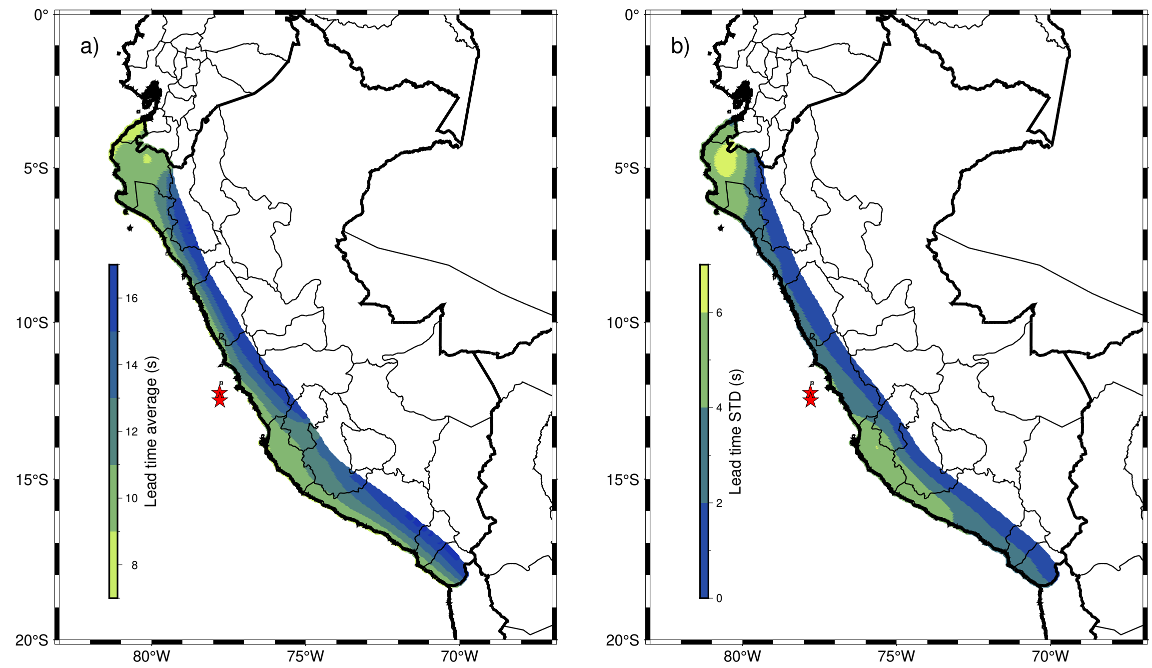

Figure 10. User lead times in the coastal region of Peru for synthetic earthquakes located within 100 km of each point and shallower than 100 km. The colors indicate the mean lead times (a) and their standard deviations (b). Red stars mark the locations of two historic earthquakes in Lima, with M 7.7 and M 7.2, both occurring in 1974.

with a lead time of 4.2 seconds. The only two events for which we obtain negative minimum lead times are two non-subduction earthquakes: the M_w 7.1 earthquake that occurred in the Peruvian rain forest in 1991 at 20 km depth (Alva-Hurtado et al., 1992) and the M_w 7.1 Macas earthquake in Ecuador in 1995, at a depth of 24 km (Alvarado et al., 1996). For these two events, the lead time at the nearest district would be negative. However, these types of earthquakes exceed magnitude 6 more rarely than subduction earthquakes, which are the focus of SASPe. Since 1970, 14% of all earthquakes shallower than 100 km with magnitudes larger than 6 were caused by off-subduction faults, and only 12% (2 earthquakes) with $M \geq 7$. Unfortunately, it is likely that E3WS misses these earthquakes (the detector would not trigger) since they are more than 200 km away from the epicenter, beyond its maximum training distance.

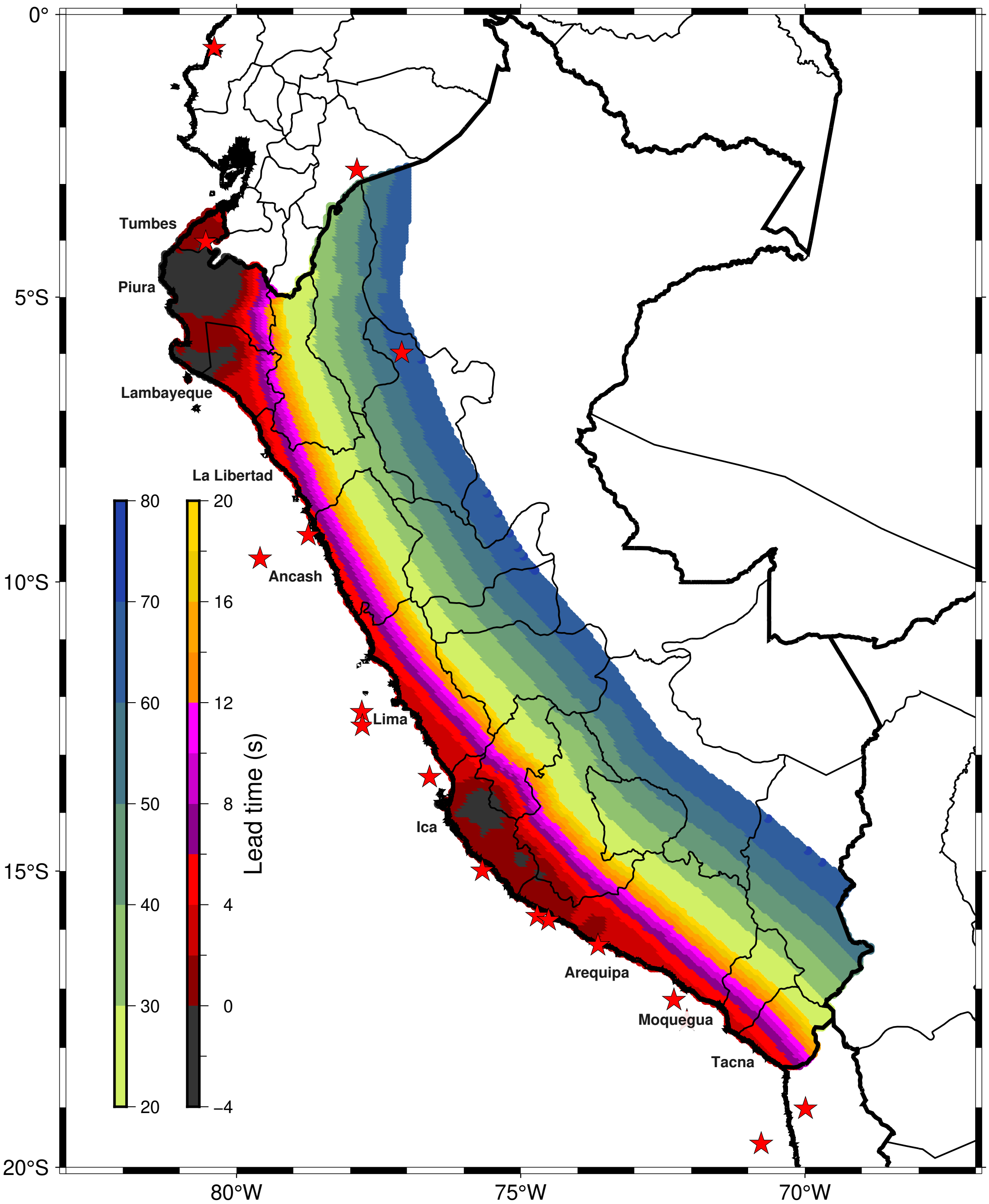

Figure 11. Worst-case-scenario user lead times for simulated subduction earthquakes (colors). Red stars denote historical M $\geq$ 7 earthquakes. Lead times are shown only for sites within the alert radius of M 9 earthquakes. Names of coastal departments are indicated.

6 Conclusion

We present the performance of the seismological components of SASPe, the newly-implemented Peruvian earthquake early warning system. The system uses the E3WS algorithm and determines its first alert using the initial 3 s of P-wave data recorded by the nearest station to the seismic source. During a testing period extending over more than 2 years, SASPe successfully detected 1,973 earthquakes with magnitudes exceeding 3. For all M $\geq$ 6 earthquakes, the estimated magnitudes are consistently larger than 6, while all estimates for earthquakes below magnitude 6 are below 6. Consequently, given the trigger threshold of M $\geq$ 6 for broadcasting alert messages, SASPe had no false positives or false negatives. SASPe enhances the location estimation of the E3WS algorithm, initially based on a single station, by incorporating data from all stations with P-wave recordings available when the closest station captures 3 seconds of earthquake records. Additionally, SASPe provides tolerances that must be added to the estimated alert radius to compensate for errors in seismic source characterization estimates, ensuring that citizens who should receive the alert message do not miss it. Continuous updates of magnitude and location estimates enable fine-tuning of the optimal alert radius. SASPe can typically generate user lead times ranging from 9 to 11 seconds for areas closest to the Peruvian coast and over 15 seconds for regions where epicentral distances exceed 94 km. In the worst-case scenarios, SASPe can provide up to 8 seconds of lead time for populations nearest to the seismic source and 10 to 20 seconds or more for regions farther away (70 to 120 km of distance). The first devices for broadcasting alert messages to the public have already been constructed in six districts of Lima, with plans for completion along the entire Peruvian coast by the year 2025.

Data and Resources

The E3WS algorithm is available at `https://github.com/PabloELara/E3WS` (last accessed June 2024). The maps were created using PyGMT (Tian et al., 2024), a Python interface for the Generic Mapping Tools (GMT), accessible at `https://www.pygmt.org` (last accessed June 2024). Data for the 2023 Guayas, Ecuador earthquake were provided by the Instituto Geofísico de la Escuela Politécnica Nacional, available at `https://www.igepn.edu.ec` (last accessed June 2024). Data for the 2023 Turkey mainshock and aftershock earthquakes were provided by The Disaster and Emergency Management Authority (AFAD), available at `https://tdvms.afad.gov.tr` (last accessed June 2024). Data for the Alaska 2023 and Marrakech 2023 earthquakes were downloaded from the Incorporated Research Institutions for Seismology (IRIS) repositories, available at `https://ds.iris.edu/` (last accessed June 2024). Data for the 2024 Noto, Japan earthquake were provided by NIED K-NET, KiK-net, National Research Institute for Earth Science and Disaster Resilience, `DOI:10.17598/NIED.0004` available at `https://www.kyoshin.bosai.go.jp/` (last accessed June 2024). SASPe data are not open to the public but are available upon request to the IGP. Supplementary material includes Figures S1 to S5. Fig. S1 shows the number of stations recording a P wave in the 3 seconds following the arrival at the nearest station. Fig. S2 shows residuals in back-azimuth using different P-wave windows (from 0.1 seconds to 3 seconds). Fig. S3 shows the dependence of the tolerances on the alert radius based on magnitude, location, and depth residuals. Figs. S4 and S5 show the performance of SASPe during the 2023 M 6.8 Ecuador earthquake and the 2022 M 6.1 Piura earthquake, respectively.

Declaration of Competing Interests

The authors acknowledge there are no conflicts of interest recorded.

Acknowledgments

This work is part of the scientific research development conducted by the Instituto Geofísico del Perú (IGP) to strengthen the "Sistema de Alerta Sísmico Peruano (SASPe)" project, funded by the Peruvian government. It has received funding from the European Research Council (ERC) under the European Union's Horizon 2020 research and innovation program (Grant Agreement 949221). This work was granted access to the HPC resources of IDRIS under the allocations AD011012142, AP011012536, A0101012314, A0121012314, AP011012126 and AD011012142R1 made by GENCI. It has been supported by the French government through the UCAJEDI Investments in the Future project (ANR-15-IDEX-01) managed by the National Research Agency (ANR) and through a graduate fellowship from the Institut de Recherche pour le Développement (IRD).

References

Abrahamson, N., Gregor, N., & Addo, K. (2016). Bc hydro ground motion prediction equations for subduction earthquakes. *Earthquake Spectra*, *32*(1), 23–44.

Alva-Hurtado, J., Meneses, J., Chang, L., Lara, J., & Nishimura, T. (1992). Ground effects caused by the alto mayo earthquakes in peru. In *Earthquake engineering, tenth world conference, balkema, rotterdam.*

Alvarado, A., Segovia, M., Yepes, H., Guillier, B., Chatelain, J.-L., Egred, J., ... Santacruz, R. (1996). The mw 6.8 macas earthquake in the subandean zone of ecuador, october 3, 1995. *Third ISAG*, 129–132.

Atkinson, G. M., & Boore, D. M. (2003). Empirical ground-motion relations for subduction-zone earthquakes and their application to cascadia and other regions. *Bulletin of the Seismological Society of America*, *93*(4), 1703–1729.

Böse, M., Allen, R., Brown, H., Gua, G., Fischer, M., Hauksson, E., ... others (2014). Cisn shakealert: An earthquake early warning demonstration system for california. In *Early warning for geological disasters* (pp. 49–69). Springer.

Böse, M., Hauksson, E., Solanki, K., Kanamori, H., Wu, Y.-M., & Heaton, T. (2009). A new trigger criterion for improved real-time performance of onsite earthquake early warning in southern california. *Bulletin of the Seismological Society of America*, *99*(2A), 897–905.

Bossu, R., Finazzi, F., Steed, R., Fallou, L., & Bondár, I. (2022). "shaking in 5 seconds!"—performance and user appreciation assessment of the earthquake network smartphone-based public earthquake early warning system. *Seismological Society of America*, *93*(1), 137–148.

Brown, H. M., Allen, R. M., Hellweg, M., Khainovski, O., Neuhauser, D., & Souf, A. (2011). Development of the elarms methodology for earthquake early warning: Realtime application in california and offline testing in japan. *Soil Dynamics and Earthquake Engineering*, *31*(2), 188–200.

Calais, E., Symithe, S., Monfret, T., Delouis, B., Lomax, A., Courboulex, F., ... others (2022). Citizen seismology helps decipher the 2021 haiti earthquake. *Science*, *376*(6590), 283–287.

Chlieh, M., Perfettini, H., Tavera, H., Avouac, J.-P., Remy, D., Nocquet, J.-M., ... Bonvalot, S. (2011). Interseismic coupling and seismic potential along the central andes subduction zone. *Journal of Geophysical Research: Solid Earth*, *116*(B12).

Chung, A. I., Henson, I., & Allen, R. M. (2019). Optimizing earthquake early warning performance: Elarms-3. *Seismological Research Letters*, *90*(2A), 727–743.

Dutilleul, P., Genest, C., & Peng, R. (2024). Bootstrapping for parameter uncertainty in the space–time epidemic-type aftershock sequence model. *Geophysical Journal International*, *236*(3), 1601–1608.

Fallou, L., Finazzi, F., & Bossu, R. (2022). Efficacy and usefulness of an independent public earthquake early warning system: A case study—the earthquake network initiative in peru. *Seismological Society of America*, *93*(2A), 827–839.

Hayes, G. P., Moore, G. L., Portner, D. E., Hearne, M., Flamme, H., Furtney, M., & Smoczyk, G. M. (2018). Slab2, a comprehensive subduction zone geometry model. *Science*, *362*(6410), 58–61.

Lara, P., Bletery, Q., Ampuero, J.-P., Inza, A., & Tavera, H. (2023). Earthquake early warning starting from 3 s of records on a single station with machine learning. *Journal of Geophysical Research: Solid Earth*, *128*(11), e2023JB026575.

Montenegro Folleco, J. A. (2023). *Estimación de características de un sismo por medio de técnicas de aprendizaje automático a partir de una sola estación* (Bachelor's Thesis). Universidad de los Andes.

Nakamura, Y. (1988). On the urgent earthquake detection and alarm system (uredas). In *Proc. of the 9th world conference on earthquake engineering* (Vol. 7, pp. 673–678).

Nakamura, Y., & Saita, J. (2007). Uredas, the earthquake warning system: Today and tomorrow. *Earthquake early warning systems*, 249–281.

Nakamura, Y., Saita, J., & Sato, T. (2011). On an earthquake early warning system (eew) and its applications. *Soil Dynamics and Earthquake Engineering*, *31*(2), 127–136.

Noda, S., Yamamoto, S., Sato, S., Iwata, N., Korenaga, M., & Ashiya, K. (2012). Improvement of back-azimuth estimation in real-time by using a single station record. *Earth, planets and space*, *64*, 305–308.

Pulido, N., Aguilar, Z., Tavera, H., Chlieh, M., Calderón, D., Sekiguchi, T., ... Yamazaki, F. (2015). Scenario source models and strong ground motion for future mega-earthquakes: Application to lima, central peru. *Bulletin of the Seismological Society of America*, *105*(1), 368–386.

Ruhl, C., Melgar, D., Chung, A., Grapenthin, R., & Allen, R. (2019). Quantifying the value of real-time geodetic constraints for earthquake early warning using a global seismic and geodetic data set. *Journal of Geophysical Research: Solid Earth*, *124*(4), 3819–3837.

Tian, D., Uieda, L., Leong, W. J., Fröhlich, Y., Schlitzer, W., Grund, M., ... Wessel, P. (2024, May). *PyGMT: A Python interface for the Generic Mapping Tools.* Zenodo. Retrieved from `https://doi.org/10.5281/zenodo.11062720` doi: 10.5281/zenodo.11062720

Villegas-Lanza, J. C., Chlieh, M., Cavalié, O., Tavera, H., Baby, P., Chire-Chira, J., & Nocquet, J.-M. (2016). Active tectonics of peru: Heterogeneous interseismic coupling along the nazca megathrust, rigid motion of the peruvian sliver, and subandean shortening accommodation. *Journal of Geophysical Research: Solid Earth*, *121*(10), 7371–7394.

Youngs, R., Chiou, S.-J., Silva, W., & Humphrey, J. (1997). Strong ground motion attenuation relationships for subduction zone earthquakes. *Seismological research letters*, *68*(1), 58–73.

Zhao, J. X., Zhang, J., Asano, A., Ohno, Y., Oouchi, T., Takahashi, T., ... others (2006). Attenuation relations of strong ground motion in japan using site classification based on predominant period. *Bulletin of the Seismological Society of America*, *96*(3), 898–913.

Implementation of the Peruvian Earthquake Early Warning System

Pablo Lara[1,2], Hernando Tavera[2], Quentin Bletery[1], Jean-Paul Ampuero[1],

Adolfo Inza[2], David Portugal[2], Benazir Orihuela[3], and Fernando Meza[2]

[1]Observatoire de la Côte d'Azur, Université Côte d'Azur, IRD, CNRS, Géoazur, France

[2]Instituto Geofísico del Perú, Lima, Perú

[3]Swiss Seismological Service at ETH Zurich, Zurich, Switzerland

Contents of this file

1. Figures S1 to S5.

1. Introduction

This supporting information includes 5 supplementary figures used in this work.

2. Figures

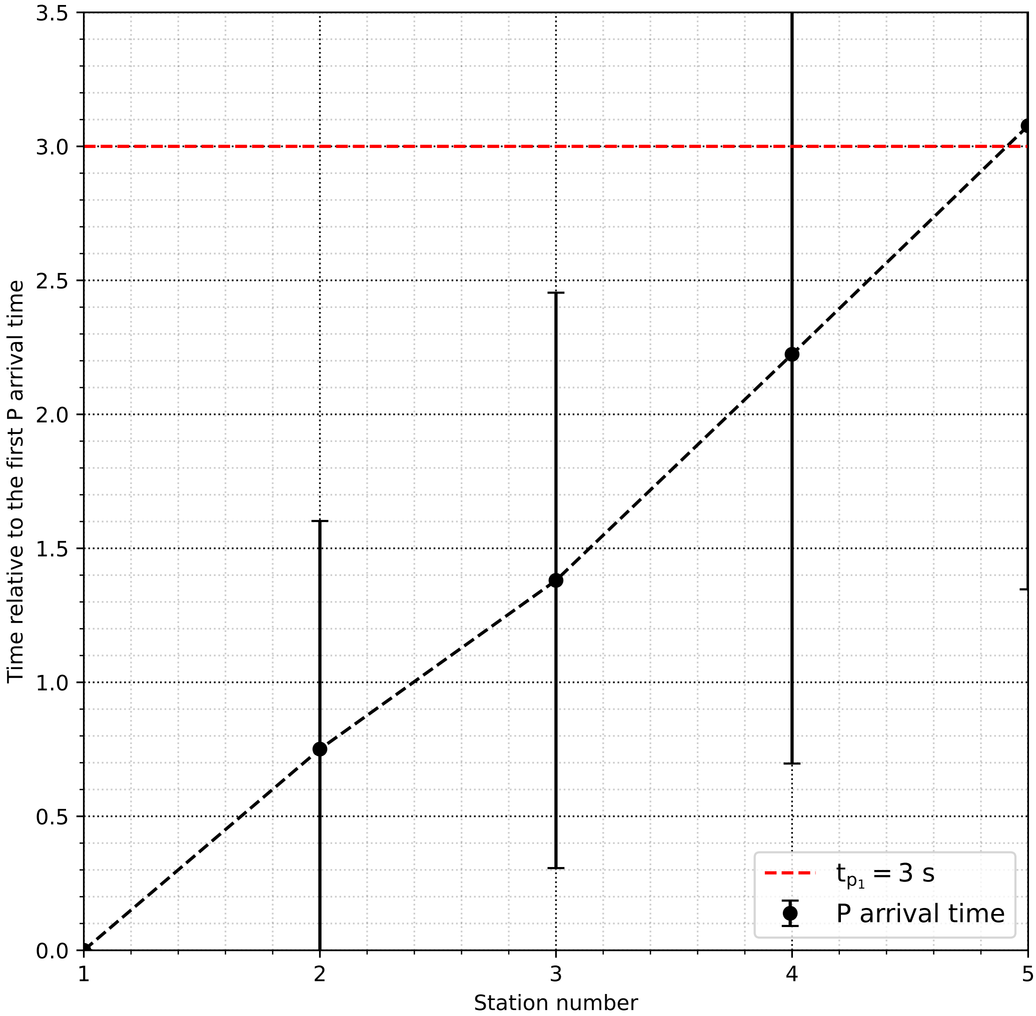

Figure S1. Number of stations recording a P wave in the 3 seconds following the arrival on the nearest station.

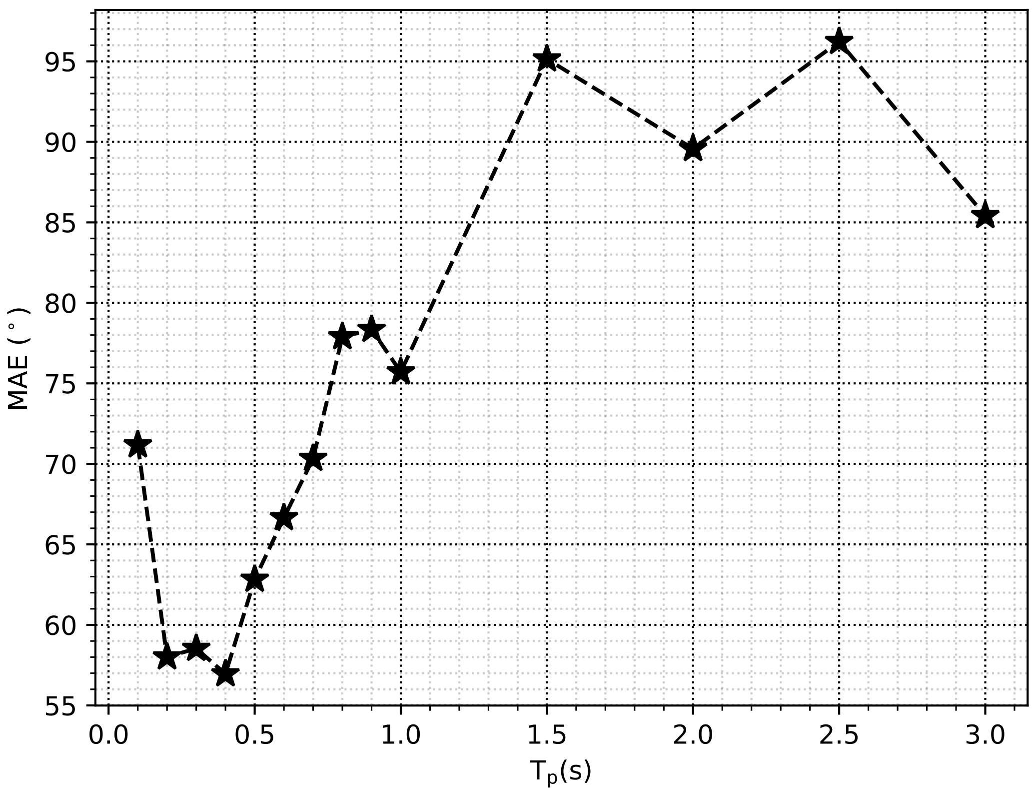

Figure S2. Residuals in back-azimuth using different P-wave windows.

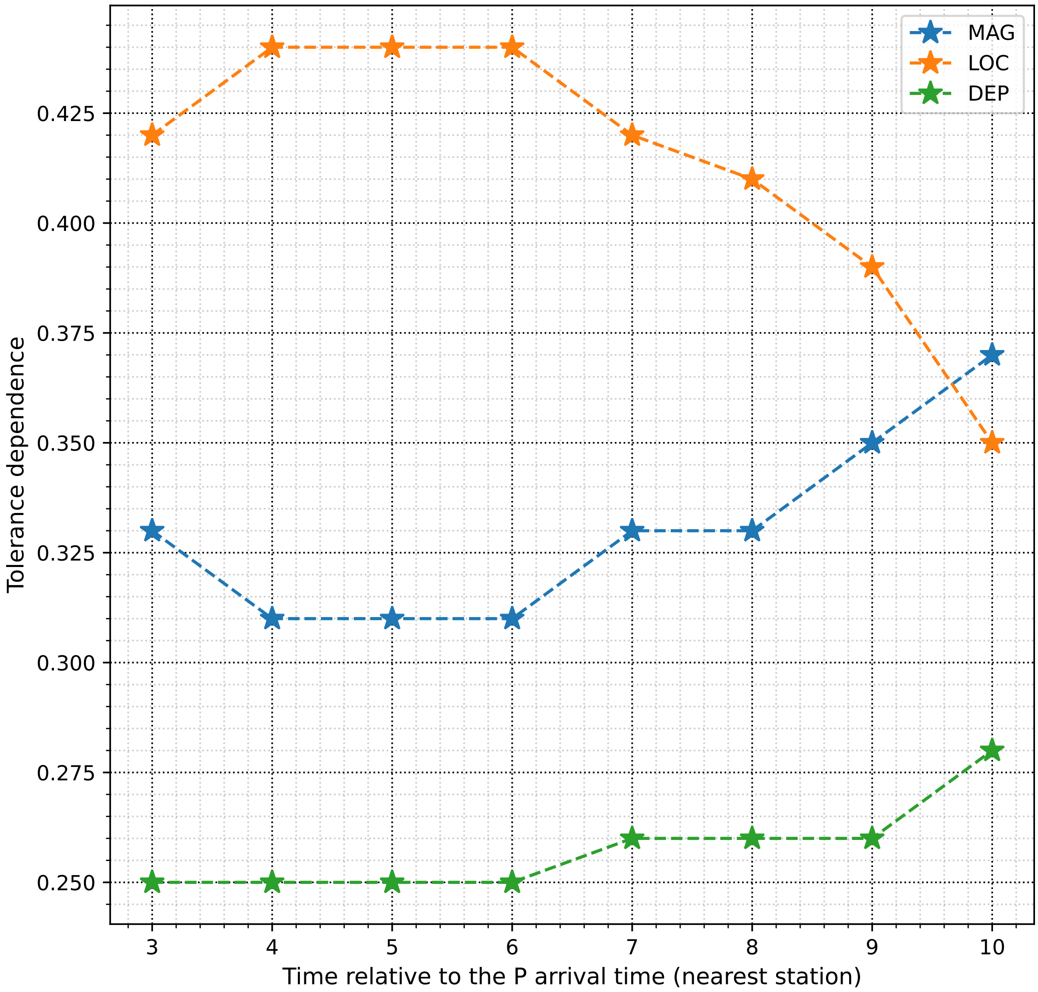

Figure S3. Tolerances dependence on magnitude, epicentral location (epicentral distance and back-azimuth), and depth spanning 3 to 10 seconds of P-wave data. Dependencies derived from equation 1. Each dependence is normalized by dividing it by the total sum.

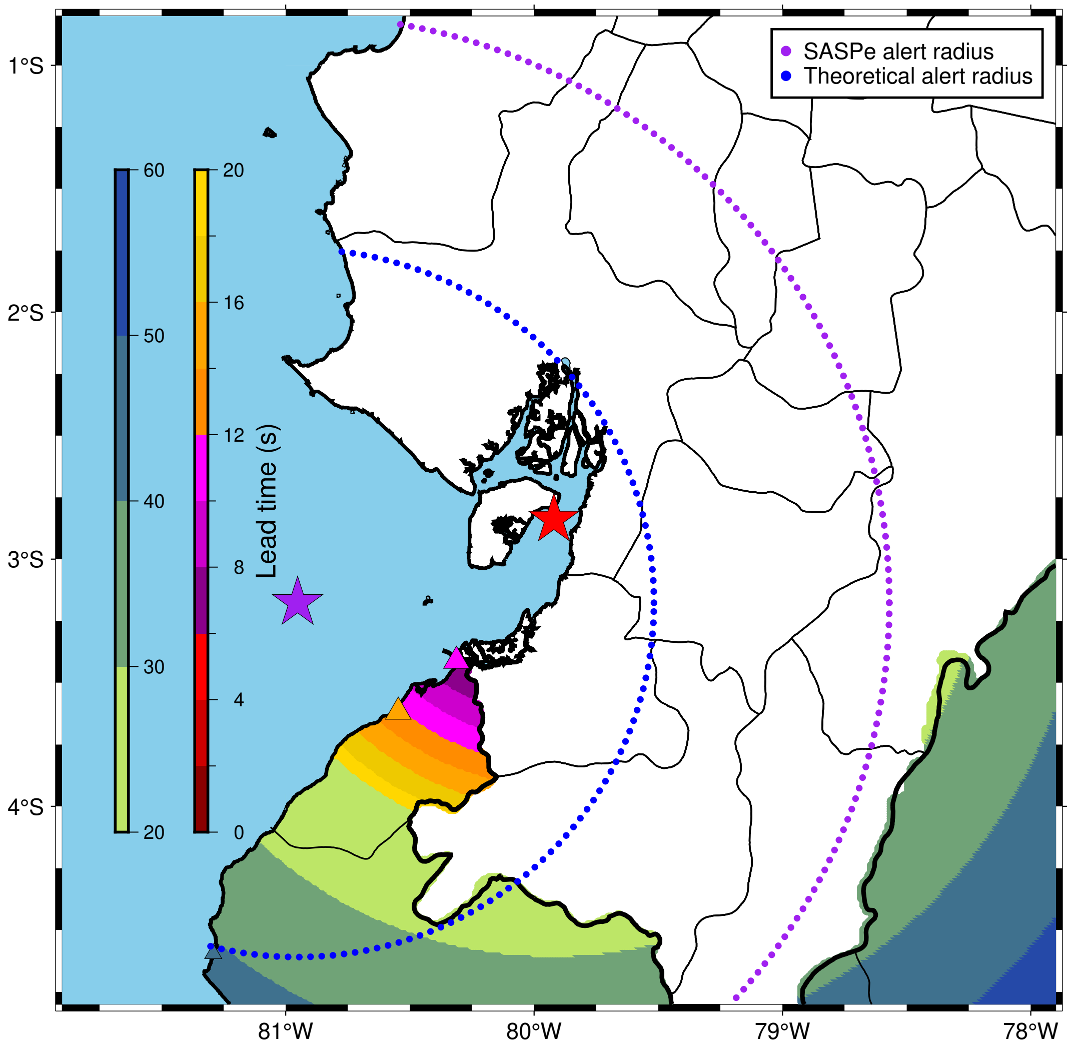

Figure S4. SASPe performance during the M6.8 earthquake in Ecuador on March 18, 2023. SASPe stations are depicted as triangles. Small red circles indicate stations with PGA values exceeding 5%g. User lead times are color-coded based on the color bar. Theoretical alert radius and SASPe-issued alert radius are shown in blue and purple circles, respectively. The red star denotes the true epicenter, while the purple star represents the estimated epicenter.

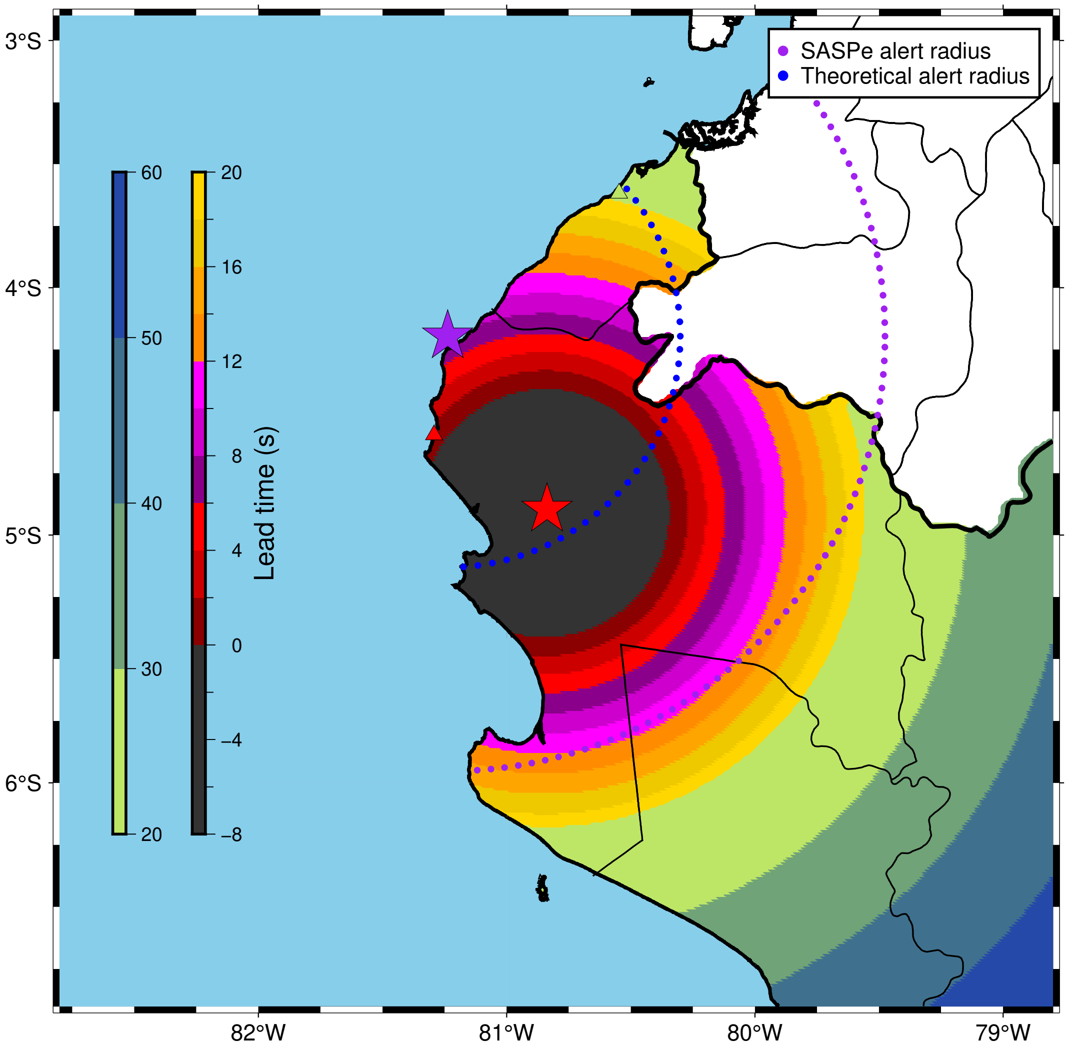

Figure S5. Same as Fig. S4, but for the M6.1 earthquake in Piura, Peru, on October 5, 2022.